

## 3D Visualization of cyanobacterial biofilms using micro-computed tomography with contrast-enhancing staining agents

Laurenz Schröer<sup>a,b,\*</sup>, Tim Balcaen<sup>c,d,e</sup>, Karel Folens<sup>b</sup>, Nico Boon<sup>b</sup>, Tim De Kock<sup>f</sup>, Greet Kerckhofs<sup>c,d,g</sup>, Veerle Cnudde<sup>a,h</sup>

<sup>a</sup> PProGress-UGCT, Department of Geology, Ghent University, Belgium

<sup>b</sup> Center for Microbial Ecology and Technology (CMET), Department of Biotechnology, Ghent University, Belgium

<sup>c</sup> Institute of Mechanics, Materials, and Civil Engineering (iMMC), UCLouvain, Belgium

<sup>d</sup> Institute of Experimental and Clinical Research (IREC), UCLouvain, Belgium

<sup>e</sup> Sustainable Chemistry of Molecules and Metals, Department of Chemistry, KU Leuven, Belgium

<sup>f</sup> Antwerp Cultural Heritage Sciences (ARCHES), University of Antwerp, Belgium

<sup>g</sup> Prometheus, Division of Skeletal Tissue Engineering, Department of Materials Engineering, KU Leuven, Belgium

<sup>h</sup> Environmental Hydrogeology, Department of Earth Sciences, Utrecht University, the Netherlands

### ARTICLE INFO

#### Keywords:

Contrast agents

μCT

Contrast-enhanced computed tomography

Microbial mats

Isotonic Lugol

Hf-WD 1:2 POM

### ABSTRACT

Currently, biofilms colonizing surfaces are mainly imaged in 2D by conventional techniques, such as optical or scanning electron microscopy. Confocal laser scanning microscopy or optical coherence tomography can visualize biofilms in 3D, but they suffer from a limited penetration depth and cannot visualize biofilms in opaque materials. Micro-computed tomography (μCT) can overcome these issues, but μCT cannot easily distinguish biofilm structures from water due to a lack of contrast difference. Within this research, five contrast-enhancing staining agents (CESAs) were evaluated for their staining potential of cyanobacterial biofilms, aiming to visualize these biofilms in 3D. Isotonic Lugol and 1:2 hafnium(IV)-substituted Wells-Dawson polyoxometalate (Hf-WD 1:2 POM) were the most promising, as they allowed visualization of the biofilms and revealed structures in the stained biofilms. Staining with isotonic Lugol could clearly visualize bundles of filaments within the biofilm, while Hf-WD 1:2 POM revealed a smooth biofilm. It is assumed that both CESAs have a different affinity towards the biofilms and could thus be used complementary. Monolacunary Wells-Dawson polyoxometalate (Mono-WD POM) showed moderate discrimination while staining with cationic iodinated CA4+ and Hexabrix® (Guerbet) containing anionic ioxaglate did not allow to distinctly visualize the biofilms. These results indicate that μCT, together with CESAs such as isotonic Lugol and Hf-WD 1:2 POM, can be used as a tool to image extensive biofilms or microbial mats in 3D. Further research will determine whether these CESAs are suitable for visualizing biofilms within opaque porous media.

### 1. Introduction

Around the world, mineral surfaces are colonized by microorganisms. Often, they attach to the surface and form biofilms of cells embedded in extracellular polymeric substances (EPS) [1]. It is important to visualize biofilms on and inside materials to understand their characteristics, their relationship with the substratum, and their effect on the processes occurring on and within these substrata. There are numerous microscopical techniques available to study biofilms, including light microscopy, confocal laser scanning microscopy (CLSM), optical coherence tomography (OCT), scanning electron microscopy

(SEM), cryo-SEM, environmental SEM, and atomic microscopy. Most of these techniques are limited to 2D, but CLSM and OCT preserve the 3D architecture of the biofilms. CLSM uses one or more lasers in the range of visible or ultraviolet light and allows to eliminate fluorescent signals that are out of focus [2,3]. OCT works with near-infrared light and can determine the structure of biofilms in a similar way as ultrasound due to the reflection of the radiation [4]. The main limitations of these techniques are the limited penetration depth of a few hundred μm [4,5] and the inability to visualize biofilms inside opaque materials.

CLSM and OCT are often suitable to determine biofilms colonizing outer surfaces. However, biofilms can grow thicker than the light

\* Corresponding author at: PProGress-UGCT, Department of Geology, Ghent University, Belgium.

E-mail address: [laurenz.schroer@ugent.be](mailto:laurenz.schroer@ugent.be) (L. Schröer).

<https://doi.org/10.1016/j.tmater.2024.100024>

Received 10 October 2023; Received in revised form 1 December 2023; Accepted 20 January 2024

Available online 23 January 2024

2949-673X/© 2024 The Author(s). Published by Elsevier B.V. This is an open access article under the CC BY-NC-ND license (<http://creativecommons.org/licenses/by-nc-nd/4.0/>).

penetration depth of these techniques. This can occur amongst others with cyanobacterial biofilms. When a surface is exposed to light, cyanobacteria are often pioneers in colonizing a new substratum. On these surfaces, cyanobacteria can have important effects. On rocks, cyanobacteria affect the water transport properties, cause discoloration, can induce  $\text{CaCO}_3$  precipitation, or can even make holes and penetrate the surface [6–8]. Cyanobacteria are also very abundant in the top layer of soils, where they can form biological soil crusts (biocrusts) together with green algae, lichens and mosses. Biocrusts can be found in almost any climatic region and cover about 12% of the Earth's terrestrial surface [9]. They are mainly widespread in arid regions, where they have a key function to stabilize soils with their EPS [10] and to fertilize the underground [11]. Cyanobacteria can also be present in aquatic environments, where they can be part of thick biofilms and form microbial mats consisting of horizontally stratified microbial communities. Their structure is defined by physicochemical gradients. Microbial mats can occur in hypersaline ponds, hot springs, oligotrophic environments or intertidal coastal zones [12].

To visualize biofilms whose thicknesses exceed a few hundred micrometers, micro-computed tomography ( $\mu\text{CT}$ ) can be used [13,14].  $\mu\text{CT}$  allows 3D visualization and avoids the need for sectioning, which is nowadays still performed to visualize thick biofilms or microbial mats [15,16]. 2D sectioning only partially resolves the 3D microstructure, as it is limited by its 2D nature and by a single sectioning orientation [17].  $\mu\text{CT}$  exploits X-rays that can easily penetrate opaque materials and are not hindered by the biofilms' thickness. However, the main challenge with  $\mu\text{CT}$  is the differentiation of biofilms from the liquid phase. Biofilms consist of about 97% water, and EPS is mainly composed of polysaccharides, proteins, lipids and extracellular DNA [18,19], which mainly consists of light elements such as C, H, O, N, S and P. This results in little contrast difference with the water phase as the X-ray attenuation coefficients of water and EPS are very close to each other. To overcome this problem, contrast-enhancing staining agents (CESAs) can be applied to provide contrast and visualize the biofilms. Some CESAs such as barium sulfate ( $\text{BaSO}_4$ ) [20], silver-coated microspheres [21], 1-chloronaphthalene [22,23], iron sulfate ( $\text{Fe}^{\text{II}}\text{SO}_4 \cdot 7 \text{H}_2\text{O}$ ) [24], iohexol [25] or Alcian blue [26] proved to be successful enhancing X-ray contrast. However, research is very limited and several of these CESAs have drawbacks, e.g. the mechanism of  $\text{BaSO}_4$ , silver-coated microspheres and 1-chloronaphthalene is to stain the surrounding solution as they are excluded from the biofilms. As observed in cartilage [27], it is expected that a CESA bound to the biofilm induces a higher contrast difference than when excluded. Furthermore,  $\text{BaSO}_4$  is applied to the sample as a suspension. The  $\text{BaSO}_4$  particles sediment over time, resulting in a heterogeneous distribution and a density gradient in the  $\mu\text{CT}$  images. Moreover,  $\text{BaSO}_4$  suspension is highly viscous and can alter the fluid flow. It could even lead to shear stress and biofilm detachment. Silver-coated particles have similar problems, while 1-chloronaphthalene is hydrophobic and highly toxic, which could affect the biofilm and is hazardous to work with. Advantages of  $\text{Fe}^{\text{II}}\text{SO}_4 \cdot 7 \text{H}_2\text{O}$  include that it is non-toxic and maintains the integrity of the biofilm before imaging, but it was only added during the cultivation of a biofilm in a tubular reactor [24]. Staining with iron sulfate requires a lot of preparation and might not be useful to study already full-grown biofilms or to use on microorganisms that do not oxidize ferrous iron on their own.

It is thus necessary to find other CESAs that allow visualizing biofilms using  $\mu\text{CT}$ . The CESAs should be non-destructive, bind directly to the biofilm, be easy to use and safe to work with. The study aims to find a suitable CESA to visualize biofilms in 3D and determine whether they even could be used to visualize structures within the biofilm. Finding an appropriate CESA could enable  $\mu\text{CT}$  to be used in research on extensive biofilms e.g. microbial mats, in 3D. Within this study, five CESAs were tested and compared: an isotonic Lugol's iodine solution (referred to as isotonic Lugol), Hexabrix®, Mono-WD POM, Hf-WD 1:2 POM and CA4+. These CESAs were chosen as they successfully enhanced the attenuation of different tissues, which have similar primary constituents

[28] as biofilms. These five CESAs were tested on cyanobacterial biofilms grown on a stone surface. The study outcomes can serve for future research aiming to visualize biofilms within opaque porous materials.

## 2. Materials and methods

### 2.1. Model microorganism and substratum

We used the freshwater model organism *Phormidium autumnale* ULC086 (also classified as CCALA 697), acquired from the Belgian Coordinated Collections of Microorganisms (BCCM). They are photosynthetic cyanobacteria belonging to the Oscillatoriales [29]. Members of the genus *Phormidium* are filamentous, and this strain forms irregular colonies of more or less parallel filaments (Fig. 1). *Phormidium* are widespread colonizers of porous stones and adhere with EPS on the substratum to form mat-like structures [30,31]. Due to their pigments, the biofilms are also clearly visible to the naked eye. *Phormidium autumnale* was chosen as the model organism as they form large filaments with a length of hundreds of  $\mu\text{m}$ , the ability to form microbial mats, fast growth and good durability.

As substratum, we chose Bentheim sandstone as it is a frequently investigated porous stone from the Early Cretaceous [32]. It mainly consists of quartz grains and contains only a limited amount of carbonates [33], which could precipitate the POMs [34]. Furthermore, it consists of feldspars (5%) and authigenic clay minerals (3%) as accessory minerals [33].

The biofilms of *Phormidium autumnale* were cultured on a natural stone surface of cubes of Bentheim sandstone, with a size in the order of 1 cm. The cyanobacteria were initially cultured in an Erlenmeyer using BG11+. It consisted 0.075 g/L  $\text{MgSO}_4 \cdot 7 \text{H}_2\text{O}$ , 0.036 g/L  $\text{CaCl}_2 \cdot 2 \text{H}_2\text{O}$ , 0.006 g/L  $\text{C}_6\text{H}_8\text{O}_7 \cdot \text{H}_2\text{O}$ , 0.001 g/L EDTA  $\cdot 2 \text{H}_2\text{O}$  (disodium salt), 1.5 g/L  $\text{NaNO}_3$ , 0.04 g/L  $\text{K}_2\text{HPO}_4 \cdot 7 \text{H}_2\text{O}$ , 0.015 g/L  $\text{NaHCO}_3$ , 0.02 g/L  $\text{Na}_2\text{CO}_3$ , 0.006 g/L  $(\text{NH}_4)_5[\text{Fe}(\text{C}_6\text{H}_4\text{O}_7)_2]$  and 1 mL/L trace element solution (2.9 g/L  $\text{H}_3\text{BO}_3$ , 1.81 g/L  $\text{MnCl}_2 \cdot 4 \text{H}_2\text{O}$ , 0.22 g/L  $\text{ZnSO}_4 \cdot 7 \text{H}_2\text{O}$ , 0.39 g/L  $\text{Na}_2\text{MoO}_4 \cdot 2 \text{H}_2\text{O}$ , 0.08 g/L  $\text{CuSO}_4 \cdot 5 \text{H}_2\text{O}$  and 0.05 g/L  $\text{Co}(\text{NO}_3)_2 \cdot 6 \text{H}_2\text{O}$ ). Cultivation occurred at room temperature under an LED strip. With a pipette, clumps of filaments bound together with EPS were inoculated on the stone samples. Hereafter, the cyanobacteria were further cultured on the bench for one week at ambient temperature. The samples were hydrated by capillary water uptake, and twice fresh BG11+ medium was added to the stone surface to provide nutrients. Illumination was again provided by an LED strip.

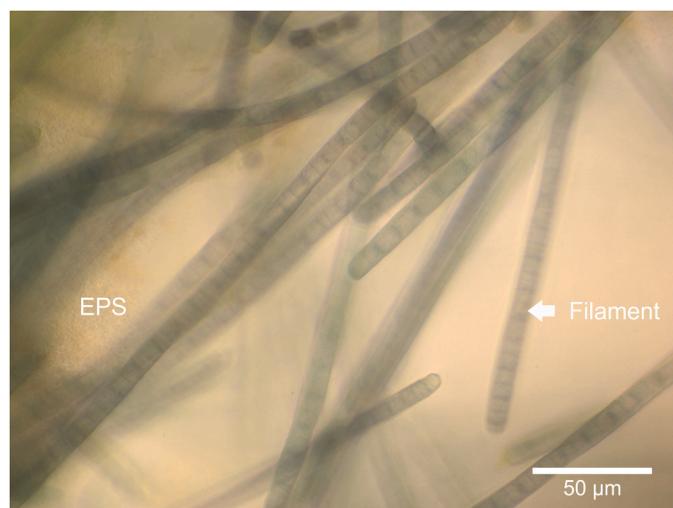


Fig. 1. Microscopic image of filaments of *Phormidium autumnale* ULC086 embedded in EPS.

## 2.2. Contrast-Enhancing Staining Agents (CESAs)

The five tested CESAs were: Isotonic Lugol, Hexabrix®, Mono-WD POM, Hf-WD 1:2 POM and CA4+. They have all been extensively used to stain biological tissues in life sciences. Lugol's iodine ( $I_2KI$ ) is one of the most frequently used CESAs for muscle tissue [35] and allows the visualization of ligaments [36]. An isotonic solution was used to limit the adverse effects of Lugol's iodine staining on the biofilms. [37,38]. Hexabrix® (Guerbet) contains the anionic ioxaglate. Due to the negative charge, its concentration depends inversely on the negative charge of the tissue. It was successfully used to image cartilage [39] and was available for clinical use [40] (but not anymore). Mono-WD POM (monolacunar Wells-Dawson polyoxometalate (POM)),  $\alpha_2\text{-K}_{10}\text{P}_2\text{W}_{17}\text{O}_{61}\cdot 20\text{H}_2\text{O}$  ( $\alpha_2\text{-P}_2\text{W}_{17}$ ) and Hf-WD 1:2 POM (1:2 hafnium(IV)-substituted Wells-Dawson POM  $\text{K}_{16}[\text{Hf}(\alpha_2\text{-P}_2\text{W}_{17}\text{O}_{61})_2]\cdot 19\text{H}_2\text{O}$ ) are two polyoxometalates (POMs) [41,42]. Previously, they have been successfully applied to enhance the contrast of murine long bones and kidneys [34]. Finally, CA4+ has a net charge of approximately four on average at pH = 7.4. It is an iodinated cationic CESA that was developed to improve potential electrostatic interactions within cartilage tissue [43–45].

## 2.3. Staining procedure

The isotonic Lugol solution was prepared by dissolving 12.948 g KI and 6.474 g  $I_2$  in 500 mL MilliQ water. Isotonic Lugol (155.99 mM KI and 51.01 mM  $I_2$ ) and Hexabrix® (320 mgI/mL, 39.3 m/V% ioxaglate meglumine and 19.6 m/V% ioxaglate sodium) were used undiluted, while the other CESAs were dissolved in Phosphate-buffered saline (PBS). This buffer is widely used in research and helps to maintain a physiological pH. Mono-WD POM and Hf-WD 1:2 POM were prepared according to the literature [34] containing a concentration of 35 g/L in which 3 g/L LiCl was added for Mono-WD POM to increase the solubility. CA4+ was prepared with a concentration of 12 g/L. One biofouled sample per CESA was immersed in the staining solution for two days at room temperature, during which the samples were gently shaken at 40 rpm. Before image acquisition, the samples were gently washed in PBS to remove (most of) the unattached CESA.

## 2.4. $\mu\text{CT}$ image acquisition and analysis

The stained samples were imaged by the HECTOR scanner at UGCT [46] using the PerkinElmer 1620 CN3 CS flat panel detector while they were submerged in PBS. The scans were taken with a voxel size of 5.5  $\mu\text{m}$  at 55 kV, 10 W and in total, 2701 projections were taken at an exposure time of 2 s/projection using one average. The projections were reconstructed with Octopus Reconstruction (XRE) [47] according to the in-house protocol during which noise, ring and beam hardening filters were applied.

Analyses were performed using ImageJ and Avizo (Thermo Fisher Scientific). For every sample, the biofilm on the top surface, the surrounding PBS and the filled pores (excluding the gas phase) were segmented over 1000 slices when the contrast difference allowed this. From every phase, the average and the standard deviation of the gray value were determined. These values were translated to attenuation coefficients based on the slope and offset in gray values of the reconstructed images. The thresholds for segmentation were manually chosen to capture the different phases in the best way. They were kept constant for all the samples, but slight variation occurred if necessary. The chosen gray values can be found in the Supplementary information (Table S1). Segmentation occurred on 3D median filtered images (26 neighborhood, 3 iterations). However, the attenuation coefficients themselves were determined on the images without extra filtering. Since there was not enough contrast difference between the biofilm and the filled pore space, and the biofilm was assumed only to colonize the outer surface of the stone, the attenuation coefficients of the filled pore space were determined after the rock phase (including the pores) was masked. This

was performed by segmenting the grains and using closing and fill holes operations. The attenuation coefficients of the biofilm and the surrounding PBS solution were determined from the inverted images excluding the stone and its pores. From these images, a subvolume was extracted containing the top of the biofilm. 3D renderings of the biofilms covering the stones were generated using VGStudio 3.3 software (Volume Graphics).

Furthermore, at a later moment, one biofouled Bentheim sample was imaged without incubation in a staining solution as a negative control. Similar settings were used at the HECTOR setup at UGCT [46] but using the XRD 4343CT detector (Varex), as the PerkinElmer detector was already replaced. The scans were taken with a voxel size of 5.5  $\mu\text{m}$  at 55 kV, 10 W and in total, 3201 projections were taken at 2 s/projection using one average. The projections were reconstructed in a similar way using Octopus Reconstruction [47].

## 3. Results and discussion

### 3.1. Screening five CESAs based on the induced contrast of the biofilm phase

Each sample was colonized with a green cyanobacterial biofilm on the top and sometimes on the sides, which was visible to the naked eye. Incubation in the different CESA solutions did not induce any visible reaction or precipitation on the biofilm or stone substratum (Fig. 2), except for the red isotonic Lugol solution, which also colored the biofilm brown/red, even after washing in PBS.

For all CESAs,  $\mu\text{CT}$  could visualize a phase that could be interpreted as the biofilm. Biofilms were interpreted as the phase on the stone surface with an attenuation higher than the surrounding PBS and gas but lower than the mineral grains. However, the contrast difference between the biofilm and the other phases varied between the CESAs. Fig. 3 shows for each CESA a cross-section through the sample parallel to the top of the Bentheim sandstone covered with biofilm. It reveals four different phases: the stone, surrounding PBS, biofilm and gas bubbles. The gas bubbles were trapped within the pores as residual gas (air) and in the biofilm phase, which most likely had a biogenic origin. Staining biofilms with isotonic Lugol (Fig. 3A) and Hf-WD 1:2 POM (Fig. 3D) induced the highest visible contrast difference between the biofilm and the surrounding phase. The biofilms were clearly visible, suggesting that scans with a shorter acquisition time using a higher energy and shorter exposure time should also be successful. The biofilm was also distinctively visible after using Mono-WD POM (Fig. 3C), and to a lesser extent, when CA4+ was used (Fig. 3E). Even without using a CESA, biofilm was visible (Fig. 3F). However, the contrast difference was very low, except on the outer side, where some highly attenuating spots were visible that could be the result of inorganic precipitates from the growth medium. The results of Hexabrix® were similar to the blank: some biofilm was visible, but the contrast was minimal (Fig. 3B). The experimental protocol might not be optimal for Hexabrix® as it might have leached out during the washing of the sample with PBS [48].

The average attenuation coefficients of the biofilm, surrounding PBS



Fig. 2. Bentheim sandstone covered with *Phormidium autumnale* two days after submergence in the different CESAs. From left to right: Isotonic Lugol, Hexabrix®, Mono-WD POM, Hf-WD 1:2 POM and CA4+.

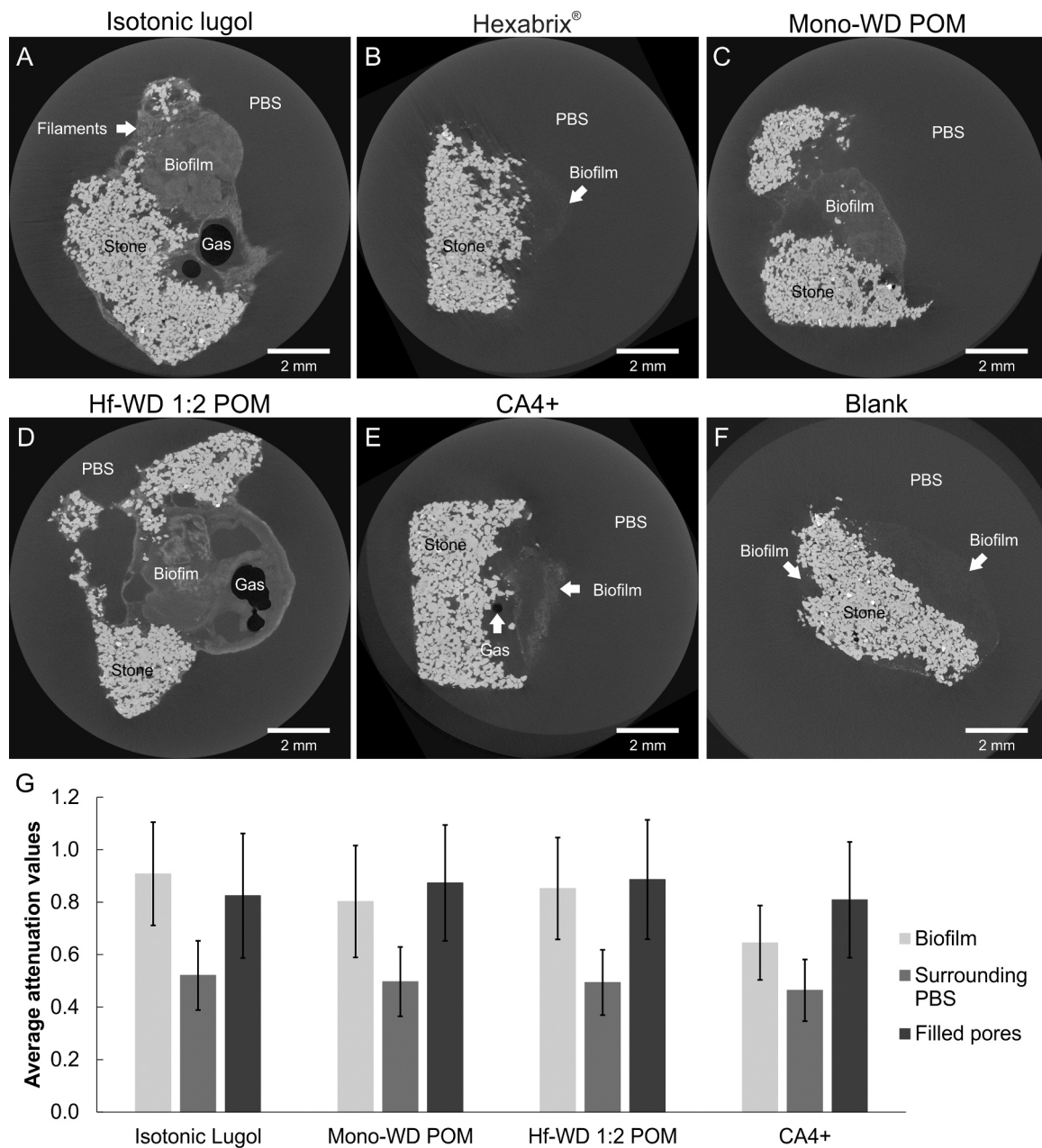


**Fig. 3.** Horizontal  $\mu$ CT cross-sections through the top surface of Bentheim sandstone covered with biofilms of *Phormidium autumnale* submerged in PBS solution. The scans were taken after staining with (A) isotonic Lugol, (B) Hexabrix®, (C) Mono-WD POM, (D) Hf-WD 1:2 POM, (E) CA4+ and (F) blank, visualizing the phases interpreted as PBS, stone, biofilm and gas. Using ImageJ, the brightness/contrast was adjusted and a median filter (radius = 2 pixels) was applied to enhance the visualization. (G) The average attenuation coefficients and standard deviation within the different phases for each sample ( $n = 1$ ) of the biofilm, surrounding PBS and filled pores (excluding the gas phase).

and the filled pores (excluding residual gas bubbles in the pore space) phases were determined. However, the X-ray contrast difference between the biofilm and the filled pore space was small. Therefore, solely the parts of the biofilms on top of each sample with enough contrast difference were segmented. We assumed the cyanobacteria colonized the outer surface of the stone, as previous research on *Phormidium autumnale* [6] showed that the bacteria do not deeply colonize the pore space and generally remain at the surface. The results are shown in Fig. 3G (the gray values and attenuation coefficients can be found in the supplementary information Tables S2 and S3). Biofilms stained with isotonic Lugol and Hf-WD 1:2 POM had an average attenuation coefficient respectively 74% and 73% higher than the surrounding PBS. Mono-WD POM and CA4+ also increased the attenuation of the biofilm

but to a lesser extent, resulting in respectively 62% and 39% higher average attenuation coefficients compared to the surrounding PBS. In the case of CA4+, this number is indicative as it was hard to segment the biofilm stained with CA4+. Also, it was most likely not possible to segment the complete biofilm, making the analysis uncertain. Hexabrix® was the least successful in providing good X-ray contrast, but it might have been washed out. Biofilms were present on the samples stained with CA4+ and Hexabrix® as they were visible by the naked eye, but they could not be segmented based on attenuation differences.

Segmenting the filled pore space was complicated due to the large variety of attenuation within the pore space. It was most likely caused due to microporosity and the presence of most likely clay, which occurs in Bentheim sandstone [33]. Only a conservative segmentation was used

to avoid as much as possible the inclusion of those phases. However, overall, the pores filled with PBS still contained a higher attenuation coefficient (Fig. 3G) than the biofilms. The different attenuation within the pores are also visible in the vertical cross-sections shown in Figs. 4A and 4B. The higher attenuation coefficient within the pores could be related to the CESAs that remained in the pore system after washing or the interaction of the CESA with the material (e.g. clays). An extra scan before adding the CESA should be taken when biofilms are expected to be present in a rock or other material with such a complex pore system. It would allow us to visualize the zones where the attenuation value increased, which could be linked to the presence of biofilms. When blanks are included, it will be possible to assess if there is any interaction with the material.

### 3.2. Visualization of cyanobacterial biofilms with isotonic Lugol and Hf-WD 1:2 POM

Biofilms acquired the highest attenuation after using isotonic Lugol and Hf-WD 1:2 POM. Additionally, these CESAs revealed the biofilm differently. Isotonic Lugol visualized a heterogenous biofilm organized in clear elongated linear structures with a higher X-ray attenuation (Figs. 3A, 4C). These were similar in size and shape to the filaments of *Phormidium autumnale*. These structures were interpreted as (bundles of) cyanobacterial filaments. As far as we know, this is the first time that a laboratory-based CT system visualized cyanobacterial filaments, as previous successful visualization was limited to the use of a synchrotron source of X-rays [49]. A similar observation was made after staining

with Mono-WD POM (Fig. 3C). However, these structures were less clear, and this CESA will not be further discussed. There were also zones within the biofilm stained with isotonic Lugol that did not contain linear structures, which could be interpreted as the EPS phase (Fig. 4C). Hf-WD 1:2 POM, on the other hand, visualized a smooth biofilm with some parts containing higher X-ray attenuation (Fig. 3D). These were arranged in specific patterns and not randomly spread within the biofilm (Figs. 4B and 4D). It indicates that Hf-WD 1:2 POM visualized some internal features.

Besides visualizing features within the biofilms after using Isotonic Lugol and Hf-WD 1:2 POM, zones were identified that had a very low to almost no X-ray attenuation (Fig. 4). The zones within the biofilm with almost no attenuation were filled with trapped gas. It is assumed that this was biogenic gas consisting most likely of oxygen produced during photosynthesis or gas produced by the degradation of organic material. Such gas bubbles are commonly observed with cyanobacterial microbial mats, that could even deform sediments [50–52]. Gas was also present within the pore space, but these were residual gas bubbles trapped in the pores after submergence. Other zones within the biofilm had an attenuation similar to PBS and were interpreted as this phase. These zones looked like gaps within the biofilm phase and could result e.g. from biogenic gas production, which was filled with PBS after the gas escaped. It is mainly visible in the vertical cross-sections in Figs. 4A and 4B above the stone surface, indicated by PBS below the biofilm. It is also visible in Fig. 4C around the gas bubbles. It indicates that there was only a limited attachment of the biofilm to the stone substratum. Gaps within the biofilm could explain the easy detachment observed in previous

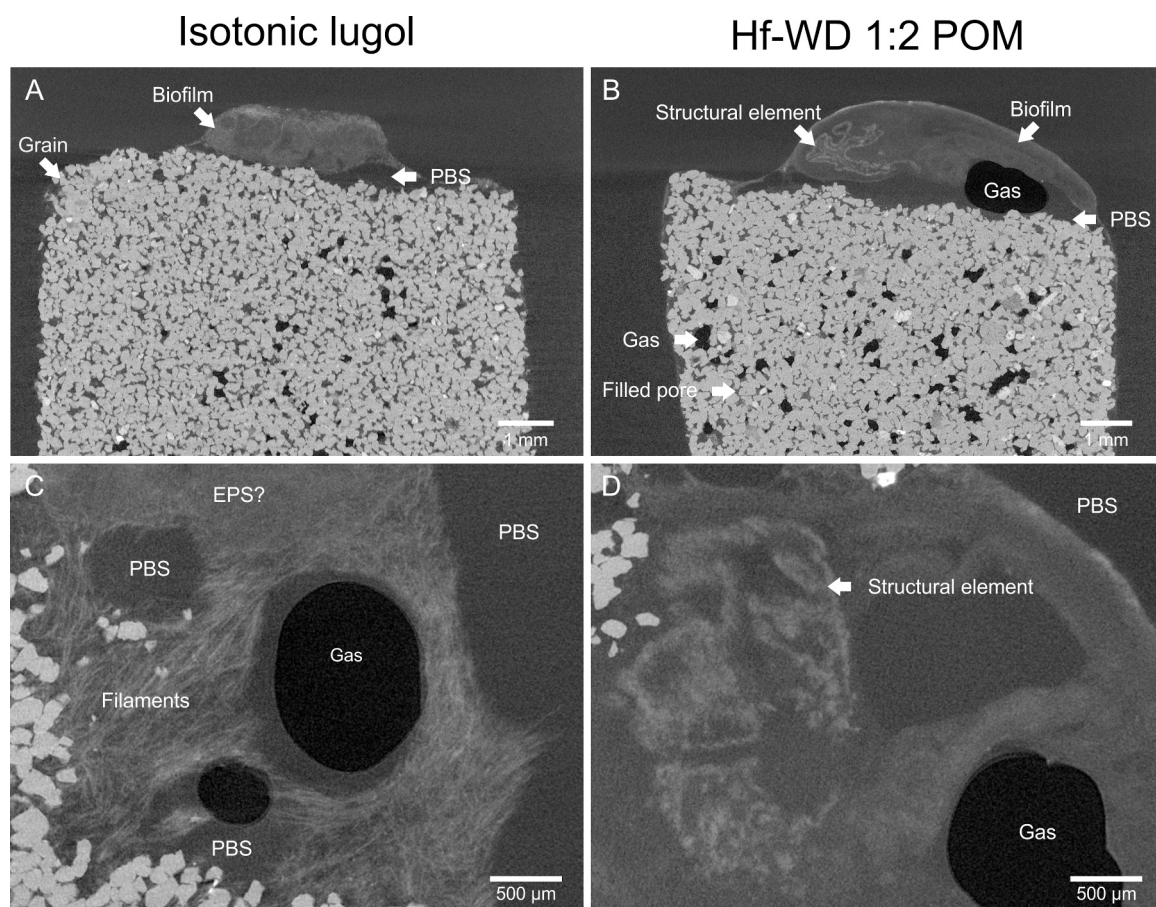


**Fig. 4.**  $\mu$ CT cross-section in the y-direction (A), (B) and zoomed horizontal cross-section (C), (D) of Bentheim sandstone covered with biofilms of *Phormidium autumnale*, submerged in PBS and stained with (A), (C) isotonic Lugol and (B), (D) Hf-WD 1:2 POM. The cross-sections show structural elements inside the biofilm and trapped (biogenic) gas. The pores of the sandstone were filled with PBS or residual gas bubbles. Some filled pores contained a relatively high attenuation, which is most likely linked to microporosity and clays. Fig. 4C shows within the biofilm filaments similar to *Phormidium autumnale* and more homogenous stained zones, interpreted as potential EPS. Using ImageJ, the brightness/contrast was adjusted to enhance the visualization, but no extra filtering was applied.

work [6]. However, we cannot exclude the possibility that some zones in the biofilms remained unstained or were potentially destained by washing.

3D rendering of the biofilms stained with isotonic Lugol and Hf-WD 1:2 POM (Fig. 5) allowed visualization of the biofilm architecture in 3D. The 3D rendering and the cut through the biofilm revealed structures when isotonic Lugol was used (Fig. 5C), which was hard to see in 2D cross-sections (Figs. 3 and 4). Furthermore, isotonic Lugol made the network of (bundles of) filaments visible (Fig. 5A). It shows that these filaments covered mainly the outside of the biofilm, while deeper the EPS phase was most likely present. It is similar to that observed with *Phormidium autumnale* under SEM during previous research [6], where the filaments were on top while EPS covered the surface. Hf-WD 1:2 POM (Figs. 5B and 5D) revealed a smooth biofilm with clear structures following the observations in Figs. 3 and 4. Overall, the structure shown after staining with Hf-WD 1:2 POM was less detailed than when isotonic Lugol was used.

### 3.3. Discussion on the interaction of isotonic Lugol and Hf-WD 1:2 POM with the biofilm

Isotonic Lugol and Hf-WD 1:2 POM led to a different visualization of the biofilm. The structures that became visible in the biofilms assume the presence of microporosity or a different composition in some parts of the biofilm to which the CESA has a different affinity. The hyperintense visualization of the bacterial filaments and some structural elements indicate that isotonic Lugol and Hf-WD 1:2 POM have increased affinity towards (some of) these structures. POMs are known to interact strongly with proteins [53], amongst others, while a plethora of interaction mechanisms for iodine species, present in Lugol's iodine solution, with biomolecules (e.g. lipids [54], proteins [55] and polysaccharides [56]) exist. Moreover, Fig. 4 indicates that the affinity differs for different regions within the biofilm for the different CESAs. It suggests that both CESAs might be used complementary to each other. In the case of isotonic Lugol staining, the clear visualization of filaments could be the result of a synergistic effect between an increased affinity of iodine

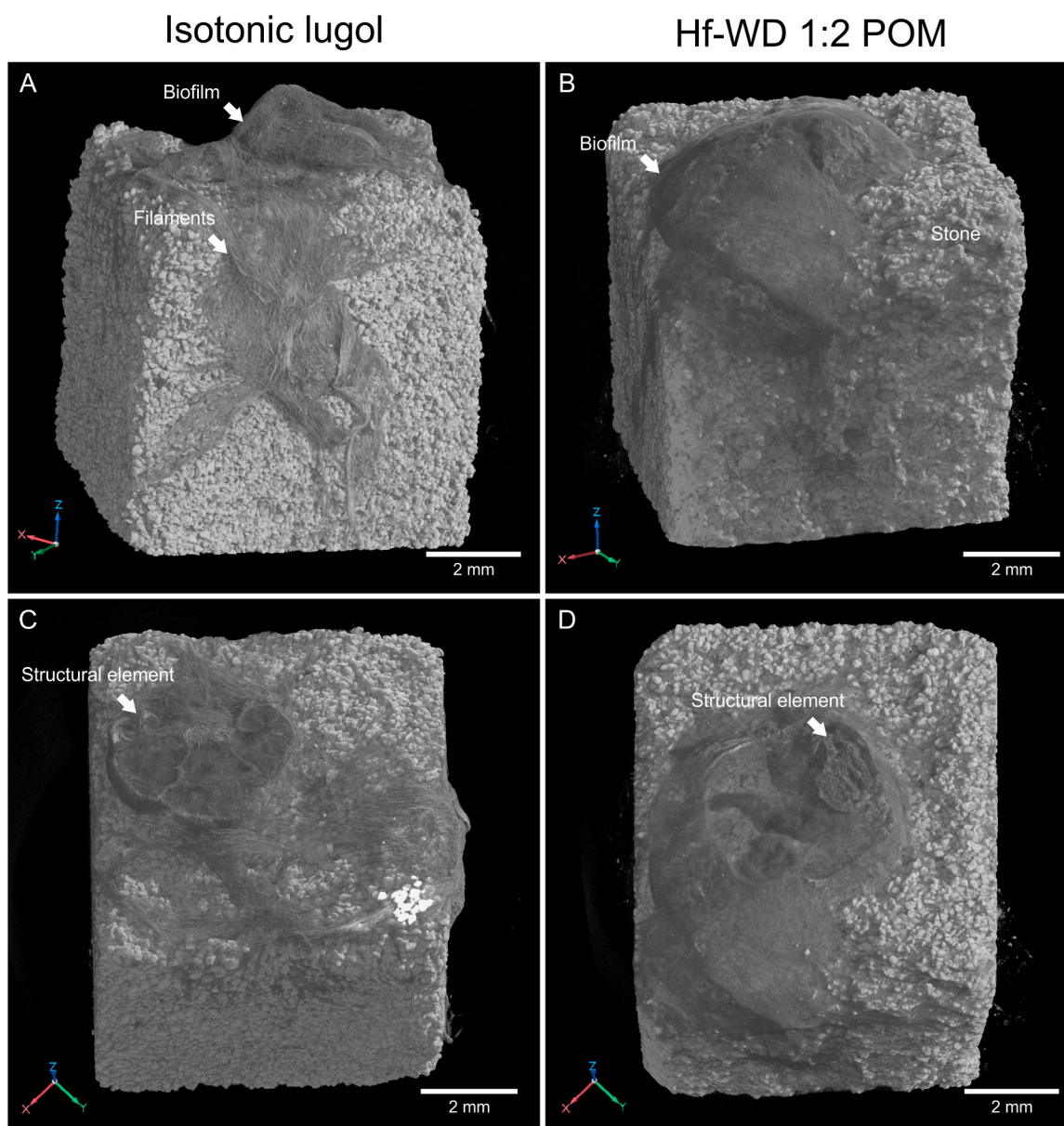


Fig. 5. 3D rendered volumes showing Bentheim covered with biofilms in which the PBS and gas bubbles were made invisible. (A) and (C) show a biofilm with (bundles of) filaments stained with isotonic Lugol, while (B) and (D) show a biofilm after staining with Hf-WD 1:2 POM. (C) and (D) show a render where a cut was made through the biofilm on top, revealing structural elements.

components for the filaments and a potential shrinkage of the EPS and filaments [57,58]. Shrinkage could occur despite the isotonicity of the Lugol [38]. Shrinkage could increase the space between the filaments and could enhance visualization. However, it might alter the structure and would be a limitation when quantitative observations are required. In the case of Hf-WD 1:2 POM staining, the filaments were not clearly visible, but some structures became hyperintense. Hf-WD 1:2 POM could cause swelling [38], which was also reflected in the fact that a smooth surface was obtained upon staining with this CESA. It might make it more difficult to distinguish biofilms within water and for quantitative analysis of the biofilms. However, Hf-WD 1:2 POM might preserve the structure better. It is worth studying if freezing opens the spaces between filaments and enhances visualization using cryogenic contrast-enhanced  $\mu$ CT, as described by Maes *et al.* [38].

#### 4. Conclusions and future perspectives

Five CESAs were tested, aiming to non-destructively visualize cyanobacterial biofilms in 3D using  $\mu$ CT in a lab environment. Isotonic Lugol and Hf-WD 1:2 POM were the most promising CESAs, as the stained biofilms were visible using  $\mu$ CT and had the highest contrast compared with the surrounding PBS solution. Moreover, they revealed structural elements within the biofilm that would have remained otherwise invisible. For isotonic Lugol, these included the clear visualization of cyanobacterial filaments, which were (in our knowledge) visualized for the first time with lab-based  $\mu$ CT. Furthermore, Both CESAs seem to have different affinities towards the biofilms and could be used complementary. Besides these two CESAs, Mono-WD POM resulted in a moderate contrast enhancement. The effects of Hexabrix® and CA4+ during these experiments were limited, as the biofilms remained hardly visible, and it seemed not to stain the complete biofilm. Overall, the results showed that  $\mu$ CT provides new opportunities to image microbial mats and thick biofilms in 3D in a lab infrastructure without the need to section the biofilms. They are also promising to visualize biofilms in opaque materials in 3D.

Future research should focus on the interaction of these CESAs with biofilms and the alterations, including shrinkage and swelling, they might cause. Moreover, it should be tested if isotonic Lugol and Hf-WD 1:2 POM interact differently with other groups of bacteria and can show e.g. the structure within heterogenous communities within microbial mats. Future work could also focus on the optimization of the staining protocol, e.g. washing the sample in PBS might not be ideal for all studied CESAs. Furthermore, these CESAs should be tested on heterotrophic bacteria colonizing the inner pore space of opaque materials, as their presence remains difficult to visualize, just as the interaction between the CESA and the porous material itself. If successful, these CESAs can help our understanding of the effects of biofilms in geological or industrial processes and even be applied in the medical field.

#### CRedit authorship contribution statement

**Kerckhofs Greet:** Conceptualization, Methodology, Resources, Writing – original draft, Writing – review & editing, Validation. **Cnudde Veerle:** Conceptualization, Funding acquisition, Methodology, Project administration, Resources, Supervision, Validation, Writing – original draft, Writing – review & editing. **Schröer Laurenz:** Conceptualization, Data curation, Formal analysis, Investigation, Methodology, Software, Validation, Visualization, Writing – original draft, Writing – review & editing. **Balcaen Tim:** Investigation, Methodology, Validation, Writing – original draft, Writing – review & editing. **Folens Karel:** Validation, Writing – original draft, Writing – review & editing. **Boon Nico:** Conceptualization, Funding acquisition, Supervision, Writing – original draft, Writing – review & editing, Resources. **De Kock Tim:** Conceptualization, Funding acquisition, Methodology, Resources, Supervision, Writing – original draft, Writing – review & editing, Validation.

#### Declaration of Competing Interest

The authors declare that they have no known competing financial interests or personal relationships that could have appeared to influence the work reported in this paper.

#### Data availability

All reconstructed scans are available at the Yoda data repository of Utrecht University and accessible through <https://doi.org/10.24416/UU01-RIFW3X>.

#### Acknowledgements

We want to thank The Research Foundation – Flanders (Fonds Wetenschappelijk Onderzoek (FWO)) for funding this research with a PhD fellowship for Laurenz Schröer (11D4520N) and the Dutch Research Council NWO for funding Veerle Cnudde for the project Bug-Control (with project number VI.C.202.074) of the NWO Talent programme. We also want to thank the EXCITE network, part of the European Union's Horizon 2020 research and innovation program under grant agreement No 101005611. Furthermore, The Ghent University Special Research Fund (BOF-UGent) is acknowledged to support the UGent Core facility UGCT (BOF.COR.2022.0009) and provide funding to Karel Folens (BOF.PDO.2020.020). We want to thank the Laboratory of Organic Synthesis of Prof. Wim De Borggraeve for providing the CESAs. Moreover, we are thankful for the FWO infrastructure grant I002720N and the Le Fonds de la Recherche Scientifique (FNRS) for the FRIA grant 40008717 of Tim Balcaen. Tim Balcaen and Greet Kerckhofs acknowledge the support from an FWO project grant (G088218N). Greet Kerckhofs acknowledges the Action de Recherche Concertée (ARC 19/24–097) - Fédération Wallonie-Bruxelles. At least we are grateful for the help and advice of the BCCM and the colleagues at UGCT, including Prof. Matthieu Boone and Iván Josipovic.

#### Appendix A. Supporting information

Supplementary data associated with this article can be found in the online version at [doi:10.1016/j.tmater.2024.100024](https://doi.org/10.1016/j.tmater.2024.100024).

#### References

- [1] H.-C. Flemming, S. Wuerz, Bacteria and archaea on Earth and their abundance in biofilms, *Nat. Rev. Microbiol.* 17 (2019) 247–260, <https://doi.org/10.1038/s41579-019-0158-9>.
- [2] J. Azeredo, N.F. Azevedo, R. Briandet, N. Cerca, T. Coenye, A.R. Costa, M. Desvaux, G. Di Bonaventura, M. Hébraud, Z. Jaglic, M. Kačániová, S. Knöchel, A. Lourenço, F. Mergulhão, R.L. Meyer, G. Nychas, M. Simões, O. Tresse, C. Sternberg, Critical review on biofilm methods, *Crit. Rev. Microbiol.* 43 (2017) 313–351, <https://doi.org/10.1080/1040841X.2016.1208146>.
- [3] C.F. Rodrigues, J. Allkja, L. Mendes, A.S. Azevedo, Methods for the visualization of multispecies biofilms, in: K.S.D.S.E. Kaushik (Ed.), *Multispecies Biofilms*, Springer, Cham, 2023, pp. 35–78, [https://doi.org/10.1007/978-3-031-15349-5\\_2](https://doi.org/10.1007/978-3-031-15349-5_2).
- [4] S. Aumann, S. Donner, J. Fischer, F. Müller, Optical Coherence Tomography (OCT): principle and technical realization. *High Resolution Imaging in Microscopy and Ophthalmology*, Springer International Publishing, Cham, 2019, pp. 59–85, [https://doi.org/10.1007/978-3-030-16638-0\\_3](https://doi.org/10.1007/978-3-030-16638-0_3).
- [5] P. Zhang, Y.-P. Chen, J.-H. Qiu, Y.-Z. Dai, B. Feng, Imaging the microprocesses in biofilm matrices, *Trends Biotechnol.* 37 (2019) 214–226, <https://doi.org/10.1016/j.tibtech.2018.07.006>.
- [6] L. Schröer, T. De Kock, S. Godts, N. Boon, V. Cnudde, The effects of cyanobacterial biofilms on water transport and retention of natural building stones, *Earth Surf. Process Land.* 47 (2022) 1921–1936, <https://doi.org/10.1002/esp.5355>.
- [7] L. Schröer, N. Boon, T. De Kock, V. Cnudde, The capabilities of bacteria and archaea to alter natural building stones – a review, *Int. Biodeterior. Biodegrad.* 165 (2021) 105329, <https://doi.org/10.1016/j.ibiod.2021.105329>.
- [8] C.A. Crispim, C.C. Gaylarde, Cyanobacteria and biodeterioration of cultural heritage: a review, *Micro Ecol.* 49 (2005) 1–9, <https://doi.org/10.1007/s00248-003-1052-5>.
- [9] E. Rodriguez-Caballero, J. Belnap, B. Büdel, P.J. Crutzen, M.O. Andreae, U. Pöschl, B. Weber, Dryland photoautotrophic soil surface communities endangered by global change, 2018 11:3, *Nat. Geosci.* 11 (2018) 185–189, <https://doi.org/10.1038/s41561-018-0072-1>.

- [10] J. Belnap, D.A. Gillette, Vulnerability of desert biological soil crusts to wind erosion: the influences of crust development, soil texture, and disturbance, *J. Arid Environ.* 39 (1998) 133–142, <https://doi.org/10.1006/jare.1998.0388>.
- [11] S.L. Strauss, T.A. Day, F. Garcia-Pichel, Nitrogen cycling in desert biological soil crusts across biogeographic regions in the Southwestern United States, *Biogeochemistry* 108 (2012) 171–182, <https://doi.org/10.1007/s10533-011-9587-x>.
- [12] C.M. Prieto-Barajas, E. Valencia-Cantero, G. Santoyo, Microbial mat ecosystems: structure types, functional diversity, and biotechnological application, *Electron. J. Biotechnol.* 31 (2018) 48–56, <https://doi.org/10.1016/j.ejbt.2017.11.001>.
- [13] V. Cnudde, M.N. Boone, High-resolution X-ray computed tomography in geosciences: a review of the current technology and applications, *Earth Sci. Rev.* 123 (2013) 1–17, <https://doi.org/10.1016/j.earscirev.2013.04.003>.
- [14] P.J. Withers, C. Bouman, S. Carmignato, V. Cnudde, D. Grimaldi, C.K. Hagen, E. Maire, M. Manley, A. Du Plessis, S.R. Stock, X-ray computed tomography, *Nat. Rev. Methods Prim.* 1 (2021) 18, <https://doi.org/10.1038/s43586-021-00015-4>.
- [15] C.S. Chan, S.M. McAllister, A.H. Leavitt, B.T. Glazer, S.T. Krepeski, D. Emerson, The architecture of iron microbial mats reflects the adaptation of chemolithotrophic iron oxidation in freshwater and marine environments, *Front Microbiol* 7 (2016) 796, <https://doi.org/10.3389/fmicb.2016.00796>.
- [16] J. Pan, D.G. Cuadrado, N.K. Noffke, Microbial-mat colonization of modern gravel deposits in a siliciclastic coastal setting, *J. Sediment. Res.* 92 (2022) 739–750, <https://doi.org/10.2110/jsr.2022.028>.
- [17] H. Hillman, Limitations of clinical and biological histology, *Med. Hypotheses* 54 (2000) 553–564, <https://doi.org/10.1054/mehy.1999.0894>.
- [18] H.-C. Flemming, J. Wingender, U. Szewzyk, P. Steinberg, S.A. Rice, S. Kjelleberg, Biofilms: an emergent form of bacterial life, *Nat. Rev. Microbiol* 14 (2016) 563–575, <https://doi.org/10.1038/nrmicro.2016.94>.
- [19] X. Zhang, P.L. Bishop, M.J. Kupferle, Measurement of polysaccharides and proteins in biofilm extracellular polymers, *Water Sci. Technol.* 37 (1998) 345–348, [https://doi.org/10.1016/S0273-1223\(98\)00127-9](https://doi.org/10.1016/S0273-1223(98)00127-9).
- [20] Y. Davit, G. Iltis, G. Debenest, S. Veran-Tissoires, D. Wildenschild, M. Gerino, M. Quintard, Imaging biofilm in porous media using X-ray computed microtomography, *J. Microsc.* 242 (2011) 15–25, <https://doi.org/10.1111/j.1365-2818.2010.03432.x>.
- [21] G.C. Iltis, R.T. Armstrong, D.P. Jansik, B.D. Wood, D. Wildenschild, Imaging biofilm architecture within porous media using synchrotron-based X-ray computed microtomography, *Water Resour. Res.* 47 (2011), <https://doi.org/10.1029/2010WR009410>.
- [22] S. Rolland du Roscoat, J.M.F. Martins, P. Séchet, E. Vince, P. Latil, C. Geindreau, Application of synchrotron X-ray microtomography for visualizing bacterial biofilms 3D microstructure in porous media, *Biotechnol. Bioeng.* 111 (2014) 1265–1271, <https://doi.org/10.1002/bit.25168>.
- [23] T. Ivankovic, S. Rolland du Roscoat, C. Geindreau, P. Séchet, Z. Huang, J.M. F. Martins, Development and evaluation of an experimental protocol for 3-D visualization and characterization of the structure of bacterial biofilms in porous media using laboratory X-ray tomography, *Biofouling* 32 (2016) 1235–1244, <https://doi.org/10.1080/08927014.2016.1249865>.
- [24] M. Carrel, M.A. Beltran, V.L. Morales, N. Derlon, E. Morgenroth, R. Kaufmann, M. Holzner, Biofilm imaging in porous media by laboratory X-Ray tomography: Combining a non-destructive contrast agent with propagation-based phase-contrast imaging tools, *PLoS One* 12 (2017) e0180374, <https://doi.org/10.1371/journal.pone.0180374>.
- [25] P. Tang, H. Xu, W. Zhang, Y. Zhu, J. Yang, Y. Zhou, Fluid transport in porous media based on differences in filter media morphology and biofilm growth in bioreactors, *Environ. Res.* 219 (2023) 115122, <https://doi.org/10.1016/j.envres.2022.115122>.
- [26] N. Zhang, C.E.L. Thompson, I.H. Townend, K.E. Rankin, D.M. Paterson, A. J. Manning, Nondestructive 3D imaging and quantification of hydrated biofilm-sediment aggregates using X-ray microcomputed tomography, *Environ. Sci. Technol.* (2018), <https://doi.org/10.1021/acs.est.8b03997>.
- [27] P.N. Bansal, R.C. Stewart, V. Entezari, B.D. Snyder, M.W. Grinstaff, Contrast agent electrostatic attraction rather than repulsion to glycosaminoglycans affords a greater contrast uptake ratio and improved quantitative CT imaging in cartilage, *Osteoarthr. Cartil.* 19 (2011) 970–976, <https://doi.org/10.1016/j.joca.2011.04.004>.
- [28] H.Q. Woodard, D.R. White, The composition of body tissues, *Br. J. Radio.* 59 (1986) 1209–1218, <https://doi.org/10.1259/0007-1285-59-708-1209>.
- [29] K. Anagnostidis, J. Komárek, Modern approach to the classification system of cyanophytes. 3 - oscillatoriales, *algological, Stud. /Arch. Für Hydrobiol. Supplement Volumes* (1988) 327–472.
- [30] O. Strunecký, J. Komárek, J. Elster, Biogeography of phormidium autumnale (Oscillatoriales, Cyanobacteria) in western and central Spitsbergen, *Pol. Polar Res.* 33 (2012) 369–382, <https://doi.org/10.2478/v10183-012-0020-5>.
- [31] L. Tomaselli, G. Lamenti, M. Bosco, P. Tiano, Biodiversity of photosynthetic microorganisms dwelling on stone monuments, *Int. Biodeterior. Biodegrad.* 46 (2000) 251–258, [https://doi.org/10.1016/S0964-8305\(00\)00078-0](https://doi.org/10.1016/S0964-8305(00)00078-0).
- [32] J.P. Wonham, H.D. Johnson, J. Mutterlose, A. Stadler, A. Ruffell, Characterization of a shallow marine sandstone reservoir in a syn-rift setting: the Bentheim Sandstone Formation (Valanginian) of the Rührmoor field, Lower Saxony Basin, NW Germany., in: K.W. Shanley, B.F. Perkins (Eds.), *Shallow Marine and Nonmarine Reservoirs: Sequence Stratigraphy, Reservoir Architecture and Production Characteristics*, SEPM Society for Sedimentary Geology, 1997: pp. 427–448, <https://doi.org/10.5724/gcs.97.18.0427>.
- [33] A.E. Peksa, K.-H.A.A. Wolf, P.L.J. Zitha, Bentheimer sandstone revisited for experimental purposes, *Mar. Pet. Geol.* 67 (2015) 701–719, <https://doi.org/10.1016/j.marpetgeo.2015.06.001>.
- [34] S. de Bournonville, S. Vangrunderbeeck, H.G.T. Ly, C. Geeroms, W.M. De Borggraeve, T.N. Parac-Vogt, G. Kerckhofs, Exploring polyoxometalates as non-destructive staining agents for contrast-enhanced microfocus computed tomography of biological tissues, *Acta Biomater.* 105 (2020) 253–262, <https://doi.org/10.1016/j.actbio.2020.01.038>.
- [35] N.S. Jeffery, R.S. Stephenson, J.A. Gallagher, J.C. Jarvis, P.G. Cox, Micro-computed tomography with iodine staining resolves the arrangement of muscle fibres, *J. Biomech.* 44 (2011) 189–192, <https://doi.org/10.1016/j.jbiomech.2010.08.027>.
- [36] R. Balint, T. Lowe, T. Shearer, Optimal contrast agent staining of ligaments and tendons for X-ray computed tomography, *PLoS One* 11 (2016) e0153552, <https://doi.org/10.1371/journal.pone.0153552>.
- [37] S. de Bournonville, S. Vangrunderbeeck, G. Kerckhofs, Contrast-enhanced MicroCT for virtual 3D anatomical pathology of biological tissues: a literature review, *Contrast Media Mol. Imaging* 2019 (2019) 1–9, <https://doi.org/10.1155/2019/8617406>.
- [38] A. Maes, C. Pestiaux, A. Marino, T. Balcaen, L. Leysens, S. Vangrunderbeeck, G. Pyka, W.M. De Borggraeve, L. Bertrand, C. Beauloye, S. Horman, M. Wevers, G. Kerckhofs, Cryogenic contrast-enhanced microCT enables nondestructive 3D quantitative histopathology of soft biological tissues, *Nat. Commun.* 13 (2022) 6207, <https://doi.org/10.1038/s41467-022-34048-4>.
- [39] G. Kerckhofs, J. Sainz, M. Maréchal, M. Wevers, T. Van de Putte, L. Geris, J. Schrooten, Contrast-enhanced nanofocus X-ray computed tomography allows virtual three-dimensional histopathology and morphometric analysis of osteoarthritis in small animal models, *Cartilage* 5 (2014) 55–65, <https://doi.org/10.1177/1947603513501175>.
- [40] H. Lusic, M.W. Grinstaff, X-ray-computed tomography contrast agents, *Chem. Rev.* 113 (2013) 1641–1666, <https://doi.org/10.1021/cr200358s>.
- [41] A.P. Ginsberg (Ed.), *Inorganic Syntheses*, Wiley, Hoboken, NJ, USA, 1990, <https://doi.org/10.1002/9780470132586>.
- [42] C.N. Kato, A. Shinohara, K. Hayashi, K. Nomiya, Syntheses and X-ray crystal structures of Zirconium(IV) and Hafnium(IV) complexes containing monovacant Wells–Dawson and Keggin polyoxotungstates, *Inorg. Chem.* 45 (2006) 8108–8119, <https://doi.org/10.1021/ic060656e>.
- [43] M.D. Newton, S.E. Hartner, S. Timmons, N.D. Delaney, M.G. Pirrone, K.C. Baker, T. Maerz, Contrast-enhanced  $\mu$ CT of the intervertebral disc: a comparison of anionic and cationic contrast agents for biochemical and morphological characterization, *J. Orthop. Res.* 35 (2017) 1067–1075, <https://doi.org/10.1002/jor.23364>.
- [44] R.C. Stewart, A.N. Patwa, H. Lusic, J.D. Freedman, M. Wathier, B.D. Snyder, A. Guermazi, M.W. Grinstaff, Synthesis and preclinical characterization of a cationic iodinated imaging contrast agent (CA4+) and its use for quantitative computed tomography of ex vivo human hip cartilage, *J. Med. Chem.* 60 (2017) 5543–5555, <https://doi.org/10.1021/acs.jmedchem.7b00234>.
- [45] R.C. Stewart, P.N. Bansal, V. Entezari, H. Lusic, R.M. Nazarian, B.D. Snyder, M. W. Grinstaff, Contrast-enhanced CT with a high-affinity cationic contrast agent for imaging ex vivo bovine, intact ex vivo rabbit, and in vivo rabbit cartilage, *Radiology* 266 (2013) 141–150, <https://doi.org/10.1148/radiol.12112246>.
- [46] B. Masschaele, M. Dierick, D. Van Loo, M.N. Boone, L. Brabant, E. Pauwels, V. Cnudde, L. Van Hoorebeke, HECTOR: A 240kV micro-CT setup optimized for research, *J. Phys. Conf. Ser.* 463 (2013) 012012, <https://doi.org/10.1088/1742-6596/463/1/012012>.
- [47] J. Vlassenbroeck, M. Dierick, B. Masschaele, V. Cnudde, L. Van Hoorebeke, P. Jacobs, Software tools for quantification of X-ray microtomography at the UGCT, *Nucl. Instrum. Methods Phys. Res. A* 580 (2007) 442–445, <https://doi.org/10.1016/j.nima.2007.05.073>.
- [48] L.H. Jin, B.H. Choi, Y.J. Kim, H.J. Oh, B.J. Kim, X.Y. Yin, B.-H. Min, Nondestructive assessment of glycosaminoglycans in engineered cartilages using hexabrix-enhanced micro-computed tomography, *Tissue Eng. Regen. Med.* 15 (2018) 311–319, <https://doi.org/10.1007/s13770-018-0117-y>.
- [49] E. Couradeau, V.J.M.N.L. Felde, D. Parkinson, D. Uteau, A. Rochet, C. Cuellar, G. Winegar, S. Peth, T.R. Northen, F. Garcia-Pichel, In situ X-ray tomography imaging of soil water and cyanobacteria from biological soil crusts undergoing desiccation, *Front Environ. Sci.* 6 (2018) 65, <https://doi.org/10.3389/fenvs.2018.00065>, <https://www.frontiersin.org/articles/10.3389/fenvs.2018.00065/full>.
- [50] A. Cornée, M. Dickman, G. Busson, Laminated cyanobacterial mats in sediments of solar salt works: some sedimentological implications, *Sedimentology* 39 (1992) 599–612, <https://doi.org/10.1111/j.1365-3091.1992.tb02139.x>.
- [51] G. Gerdes, Structures left by modern microbial mats in their host sediments, in: J. Schieber, P.K. Bose, P.G. Eriksson, S. Banerjee, S. Sarkar, W. Altermann, O. Catuneau (Eds.), *Atlas of Microbial Mat Features Preserved within the Clastic Rock Record*, Elsevier, 2007, pp. 5–38.
- [52] G. Gerdes, T. Klenke, N. Noffke, Microbial signatures in peritidal siliciclastic sediments: a catalogue, *Sedimentology* 47 (2001) 279–308, <https://doi.org/10.1046/j.1365-3091.2000.00284.x>.
- [53] D.E. Salazar Marcano, N.D. Savić, S.A.M. Abdelhameed, F. de Azambuja, T. N. Parac-Vogt, Exploring the reactivity of polyoxometalates toward proteins: from interactions to mechanistic insights, *JACS Au* 3 (2023) 978–990, <https://doi.org/10.1021/jacsau.3c00011>.
- [54] G. Palumbo, F. Zullo, The use of iodine staining for the quantitative analysis of lipids separated by thin layer chromatography, *Lipids* 22 (1987) 201–205, <https://doi.org/10.1007/BF02537303>.
- [55] C.M. Early, A.C. Morhardt, T.P. Cleland, C.M. Milensky, G.M. Kavich, H.F. James, Chemical effects of diceCT staining protocols on fluid-preserved avian specimens, *PLoS One* 15 (2020) e0238783, <https://doi.org/10.1371/journal.pone.0238783>.

- [56] S. Moulay, Molecular iodine/polymer complexes, *J. Polym. Eng.* 33 (2013) 389–443, <https://doi.org/10.1515/polyeng-2012-0122>.
- [57] J. Buytaert, J. Goyens, D. De Greef, P. Aerts, J. Dirckx, Volume shrinkage of bone, brain and muscle tissue in sample preparation for micro-CT and Light Sheet Fluorescence Microscopy (LSFM), *Microsc. Microanal.* 20 (2014) 1208–1217, <https://doi.org/10.1017/S1431927614001329>.
- [58] P. Vickerton, J. Jarvis, N. Jeffery, Concentration-dependent specimen shrinkage in iodine-enhanced micro microCT, *J. Anat.* 223 (2013) 185–193, <https://doi.org/10.1111/joa.12068>.